arXiv:1410.6398v1 [cond-mat.str-el] 23 Oct 2014

Chirality density wave of the 'hidden order' phase in URu_2Si_2

H.-H. Kung[1,***], R. E. Baumbach[2], E. D. Bauer[2], V. K. Thorsmølle[1], W.-L. Zhang[1,†], K. Haule[1,**], J. A. Mydosh[3] & G. Blumberg[1,*]

[1]Department of Physics & Astronomy, Rutgers University, Piscataway, New Jersey 08854, USA.
[2]Los Alamos National Laboratory, Los Alamos, New Mexico 87545, USA.
[3]Kamerlingh Onnes Laboratory, Leiden University, 2300 RA Leiden, The Netherlands.
[†]On leave from Institute of Physics, Chinese Academy of Sciences, Beijing 100190, China.
To whom correspondence should be addressed, e-mails: *girsh@physics.rutgers.edu; **haule@physics.rutgers.edu; ***skung@physics.rutgers.edu.

A second-order phase transition is associated with emergence of an "order parameter" and a spontaneous symmetry breaking. For the heavy fermion superconductor URu_2Si_2, the symmetry of the order parameter associated with its ordered phase below 17.5 K has remained ambiguous despite 30 years of research, and hence is called "hidden order" (HO). Here we use polarization resolved Raman spectroscopy to specify the symmetry of the low energy excitations above and below the HO transition. These excitations involve transitions between interacting heavy uranium 5*f* orbitals, responsible for the broken symmetry in the HO phase. From the symmetry analysis of the collective mode, we determine that the HO parameter breaks local vertical and diagonal reflection symmetries at the uranium sites, resulting in crystal field states with distinct chiral properties, which order to a commensurate chirality density wave ground state.

Electrons occupying 5*f* orbitals often possess dual characters in solids, partly itinerant and partly localized, which leads to a rich variety of self-organization at low temperature, such as magnetism, superconductivity, or even more exotic states (*1*). These ordered states are in general characterized by the symmetry they break, and an order parameter may be constructed to describe the state with reduced symmetry. In a solid, the order parameter encodes the microscopic interactions among electrons that lead to the phase transition. In materials containing *f*-electrons, exchange interactions of the lanthanide or actinide magnetic moments typically generate long-range antiferromagnetic or ferromagnetic order at low temperatures, but multipolar ordering such as quadrupolar, octupolar and hexadecapolar is also possible (*2*).

One particularly interesting example among this class of materials is the uranium-based inter-metallic compound URu_2Si_2. It displays a non-magnetic second-order phase transition into an electronically ordered state at $T_{\rm HO} = 17.5\,{\rm K}$, which becomes superconducting below 1.5 K (*3, 4*). Despite numerous theoretical proposals to explain the properties below $T_{\rm HO}$ in the past 30 years (*5–10*), the symmetry and microscopic mechanism for the order parameter remains ambiguous, hence the term "hidden order" (HO) (*11*). In this ordered state, an energy gap in both spin and charge response have been reported (*12–18*). In addition, an in-gap collective excitation at a commensurate wave vector has been observed in neutron scattering experiments (*16–18*). Recently, four-fold rotational symmetry breaking under an in-plane magnetic field (*19*) and a lattice distortion along the crystallographic *a*-axis (*20*) has been reported in high quality small crystals. However, the available experimental works can not yet conclusively determine the symmetry of the order parameter in the HO phase.

URu_2Si_2 crystallizes in a body-centered tetragonal structure belonging to the $\mathbb{D}_{4\mathbb{h}}$ point group (space group No. 139 $I4/mmm$, Fig 1A). The uniqueness of URu_2Si_2 is rooted in the coexistence of the broad conduction bands, comprised mostly of Si-*p* and Ru-*d* electronic states, and more localized U-5*f* orbitals, which are in a mixed valent configuration between tetravalent

$5f^2$ and trivalent $5f^3$ (*21*). When the temperature is lowered below approximately 70 K, the hybridization with the conduction band allows a small fraction of a U-5*f* electron to participate in formation of a narrow quasiparticle band at the Fermi level, while the rest of the electron remains better described as localized on the uranium site.

In the dominant atomic configuration (*7, 22*), the orbital angular momentums and spins of the two quasi-localized U-5*f* electrons add up to total momentum $4\hbar$, having nine-fold degeneracy. In the crystal environment of URu_2Si_2, these states split into seven energy levels denoted by irreducible representations of the $\mathbb{D}_{4\mathbb{h}}$ group: 5 singlet states $2A_{1g} \oplus A_{2g} \oplus B_{1g} \oplus B_{2g}$ and 2 doublet states $2E_g$. Each irreducible representation possess distinct symmetry properties under operations such as reflection, inversion, and rotation. For example, the A_{1g} states are invariant under all symmetry operations of the $\mathbb{D}_{4\mathbb{h}}$ group (Fig. 1A), but the A_{2g} state changes sign under all diagonal and vertical reflections, and thereby possesses 8 nodes (Fig. 1A). Most of the measurable physical quantities, such as density-density and stress tensors, or one particle response functions, are symmetric under exchange of *x*- and *y*-axis in tetragonal crystal structure and therefore do not probe the A_{2g} excitations. In contrast, these A_{2g} excitations are accessible to Raman spectroscopy (*23–26*).

Raman scattering is an inelastic process which promotes excitations of controlled symmetry (*22*) (Fig. 1A) defined by the scattering geometries, namely polarizations of the incident and scattered light (*27*) (blue and red arrows in Fig. 5). It enables to separate the spectra of excitations into single symmetry representation (*23*), such as A_{1g}, A_{2g}, B_{1g}, B_{1g}, and E_g in the $\mathbb{D}_{4\mathbb{h}}$ group (Fig. 5), and thereby classify the symmetry of the collective excitations (*22*). The temperature evolution of these excitations across a phase transition provides an unambiguous identification of the broken symmetries. Unlike most other symmetry sensitive probes requiring external perturbations, such as magnetic (*19*), electric or strain fields (*28*), the photon field used by Raman probe is weak. Thus, Raman spectroscopy presents an ideal tool to study the

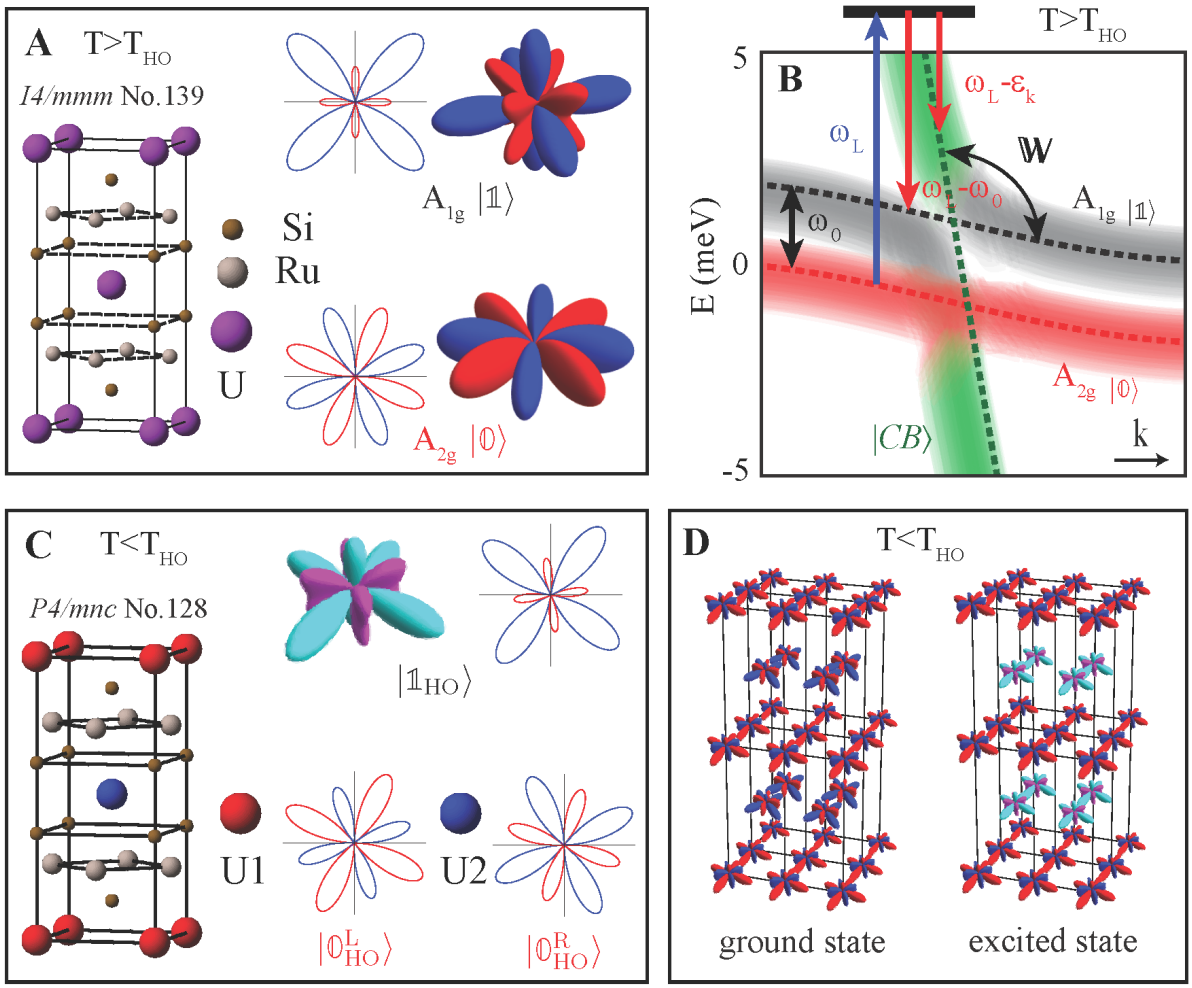

Figure 1: Schematics of the local symmetry and band structure of the quasi-localized states in the minimal model, above and below $T_{\rm HO}$. (**A**) The crystal structure of URu_2Si_2 in the paramagnetic phase. Presented in 3D and *xy*-plane cut are wave functions that show the symmetry of the A_{2g} state $|\mathbb{0}\rangle$ and A_{1g} state $|\mathbb{1}\rangle$, where the positive (negative) amplitude is denoted by red (blue) color. The A_{1g} state is symmetric with respect to the vertical and diagonal reflections, while the A_{2g} state is antisymmetric with respect to these reflections. (**B**) Schematic of the band structure of a minimal model in the paramagnetic state. The green dashed line denotes the conduction band $|CB\rangle$, the red and black dashed lines denote crystal field states of the U *5f* electrons: the ground state $|\mathbb{0}\rangle$ and the first excited state $|\mathbb{1}\rangle$ (*22*). A cartoon of the Raman process is shown, where the blue and red arrows denote the incident and scattered light, respectively. ω_L is the incoming photon energy (not in scale), $\mathbb{W}$ is the hybridization strength between $|\mathbb{1}\rangle$ and $|CB\rangle$, ω_0 and ε_k are the resonance energies for $|\mathbb{0}\rangle \rightarrow |\mathbb{1}\rangle$ and $|\mathbb{0}\rangle \rightarrow |CB\rangle$, respectively. (**C**) The crystal structure of URu_2Si_2 in the HO phase, and wave functions that show the symmetry of the chiral states $|\mathbb{0}^{\rm L}_{\rm HO}\rangle$ and $|\mathbb{0}^{\rm R}_{\rm HO}\rangle$, and the excited state $|\mathbb{1}_{\rm HO}\rangle$. The *left*- and *right*-handed states, denoted by red and blue atoms, respectively, are staggered in the lattice as shown. (**D**) Show schematics of chirality density wave, where the chiral states are staggered in the lattice (left). The right figure shows one of the possible excited state of the chirality density wave, where the chiral state $|\mathbb{0}^{\rm R}_{\rm HO}\rangle$ at lattice site U2 is excited to $|\mathbb{1}_{\rm HO}\rangle$.

broken symmetries across phase transitions without introducing external symmetry breaking perturbations.

We employ linearly and circularly polarized light to acquire the temperature evolution of the Raman response functions in all symmetry channels. In figure 2 we plot the Raman response in the A_{2g} channel, where the most significant temperature dependence was observed. The Raman response in the paramagnetic state can be described within a low energy minimal model (illustrated in Fig. 1A, B) that contains two singlet states of A_{2g} and A_{1g} symmetries, split by ω_0, and a predominantly A_{1g} symmetry conduction band. In the following, we denote the singlet states of A_{2g} and A_{1g} symmetries by $|\mathbb{0}\rangle$ and $|\mathbb{1}\rangle$, as suggested in Ref. (*7*), and conduction band labeled by $|CB\rangle$.

At high temperatures, the Raman response exhibits quasielastic scattering, with maximum decreasing from 5 meV at room temperature to 2 meV at low temperature (Fig. 2). We interpret these excitations as transitions from the $|\mathbb{0}\rangle$ state into conduction band $|CB\rangle$. Below 50 K, a new maximum around 1 meV develops. This feature resembles a Fano-type interference, where a resonance interacts with the electronic continuum (*29*). Here, we interpret the two interacting excitations as the quasielastic scattering (blue lines in Fig. 2), and an overdamped ω_0 resonance between $|\mathbb{0}\rangle$ and $|\mathbb{1}\rangle$ states (green lines in Fig. 2). After turning on the hybridization between $|\mathbb{1}\rangle$ and $|CB\rangle$, some of the Raman spectral weight is redistributed to lower energy, whereby the spectra acquires the observed feature. Such hybridization tracks the formation of the heavy fermion states in URu_2Si_2.

Figure 3 displays a comparison between the static Raman susceptibility $\chi'_{A_{2g}}(0)$ (left axis) and the *c*-axis static magnetic susceptibility χ_c^m (right axis), showing that in the paramagnetic phase the responses are proportional to each other. This proportionality can be understood by noting that both susceptibilities probe A_{2g}-like excitations, which are dominated by transitions from $|\mathbb{0}\rangle$ to conduction band $|CB\rangle$, hence in the minimal model of figure 1B, they are propor-

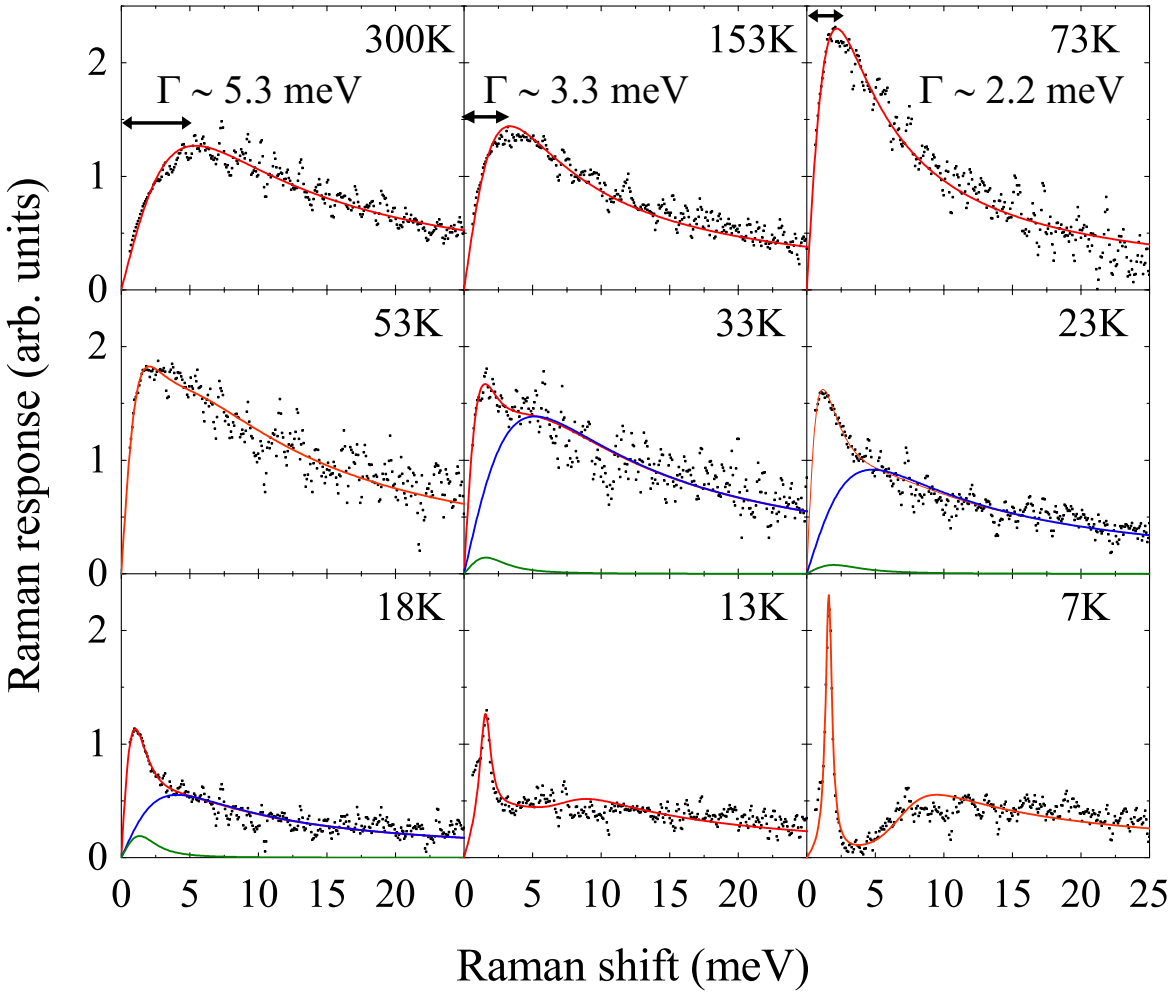

Figure 2: Temperature dependence of the Raman response in A_{2g} symmetry channel (black dots). The red lines are fitting curves to a Fano model (*29*) within the minimal model described in figure 1B: $\chi''_{A_{2g}}(\omega,T) = -\mathrm{Im}\left[\mathbf{K}^\dagger(\chi_0^{-1} - \mathbb{W})^{-1}\mathbf{K}\right]$, where $\mathbf{K}$ is the coupling amplitude to light, $\mathbb{W}$ is the off-diagonal coupling matrix between the two excitation channels, describing the hybridization process shown in figure 1B. $\chi_0 = \mathrm{Diag}\left[(i\omega - \Gamma)^{-1},\ [(\omega - \omega_0 + i\gamma)^{-1} - (\omega + \omega_0 + i\gamma)^{-1}]\right]$ is the unperturbed susceptibility. The first term is the quasielastic peak, where $\Gamma(T)$ is the peak position. The second term is a Lorentzian for a resonant transition between the quasi-localized states $|\mathbb{0}\rangle$ and $|\mathbb{1}\rangle$, with energy ω_0 and scattering rate $\gamma(T)$. From 33 to 18 K, the quasielastic peak and the overdamped ω_0 resonance are denoted by blue and green lines, respectively. The appearance of the maximum at 1 meV is due to the spectral weight redistribution resulting from the hybridization coupling $\mathbb{W}$. Below T_{HO} (7 and 13 K), the spectra show an energy gap opening and the appearance of another excitation within the gap, which sharpens dramatically upon cooling.

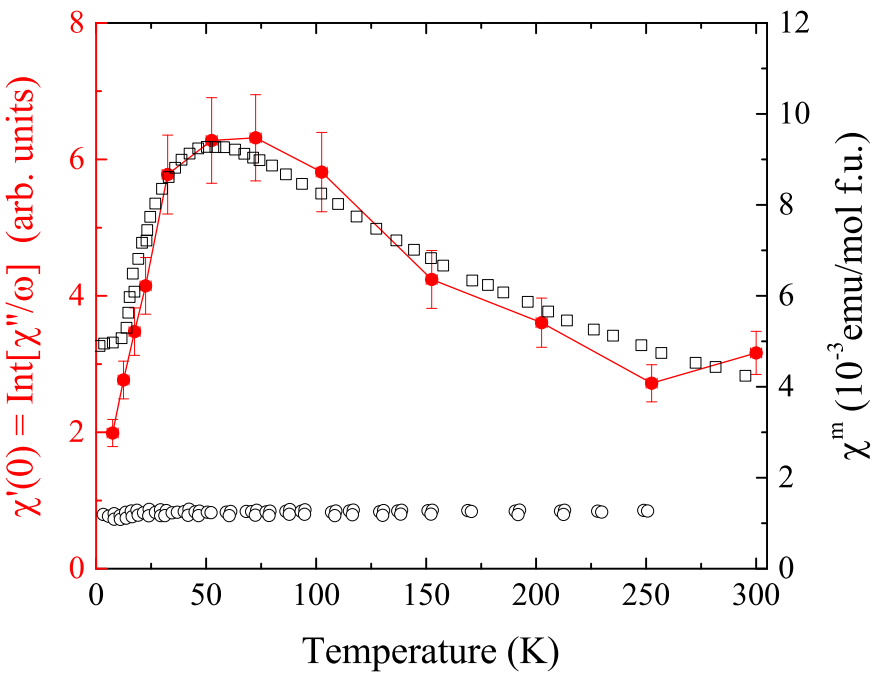

Figure 3: Comparison of static Raman and magnetic susceptibilities. Temperature dependence of the static Raman susceptibility in A_{2g} channel: $\chi'_{A_{2g}}(0,T) = \frac{2}{\pi}\int_0^\infty \frac{\chi''_{A_{2g}}(\omega,T)}{\omega}\, d\omega$ (solid dots), and the static magnetic susceptibility along *c*- and *a*-axis from Ref. (*3*) are plotted as open squares and circles, respectively.

tional to each other. The extreme anisotropy of the magnetic susceptibility (Fig. 3) also follows from this minimal model (*22*).

Below 18 K, the Raman response in the A_{2g} channel (Fig. 2) shows the suppression of low energy spectral weight below 6 meV and the emergence of a sharp in-gap mode at 1.6 meV. Figure 4 shows the detailed development of these features. The temperature dependence of the gap qualitatively follows the gap function expected from a mean-field BCS model (pink line in Fig. 4).

Having established the Raman response of A_{2g} symmetry and its correspondence with the magnetic susceptibility in the paramagnetic state, we now present our main results describing the symmetry breaking in the HO state. Figure 5 shows the Raman response in all six proper

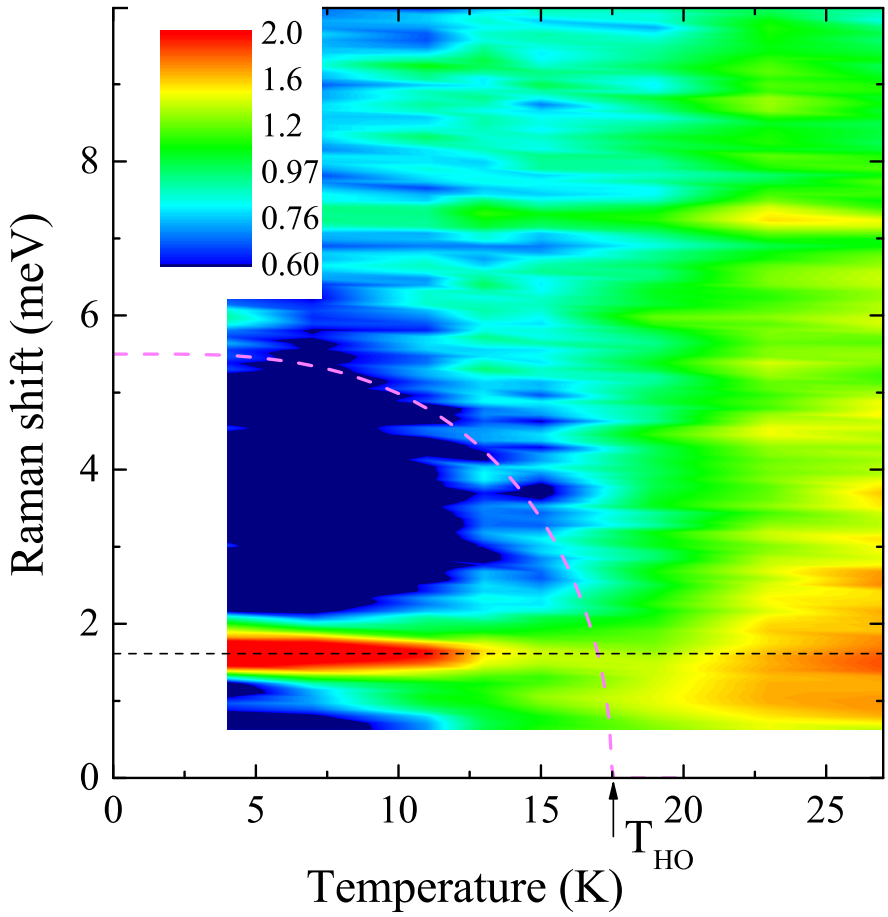

Figure 4: Raman response in the XY scattering geometry as function of temperature and Raman shift energy. The contour plot shows the temperature evolution of the low energy Raman response in the XY scattering geometry. A sharp excitation at 1.6 meV (indicated by the black dashed line) emerges below T_{HO}. The mode's full width at half maximum decreases on cooling to about 0.3 meV at 4 K. A gap-like suppression develops to a magnitude of about 6 meV at 4 K. The pink dashed line shows the temperature dependence of a gap expected from a mean-field BCS model with a transition temperature of 17.5 K.

scattering geometries at 7 K. The intense in-gap mode is observed in all scattering geometries containing A_{2g} symmetry. The mode can be interpreted as a $\omega_0 = 1.6$ meV resonance between the $|\mathbb{0}\rangle$ and $|\mathbb{1}\rangle$ quasi-localized states, which can only appear in the A_{2g} channel of the $\mathbb{D}_{4\mathbb{h}}$ group (Fig. 1B). A weaker intensity is also observed at the same energy in XX and X′X′ geometries commonly containing the excitations of the A_{1g} symmetry, and a much weaker intensity is barely seen within the experimental uncertainty in RL geometry.. The in-gap mode intensity in the A_{1g} channel is about four times weaker than in the A_{2g} channel.

The observation of this intensity "leakage" into forbidden scattering geometries implies the lowering of symmetry in the HO phase, allowing some of the irreducible representations of $\mathbb{D}_{4\mathbb{h}}$ point group to mix. For example, the ω_0 mode intensity "leakage" from the A_{2g} into the A_{1g} channel implies that the irreducible representation A_{1g} and A_{2g} of the $\mathbb{D}_{4\mathbb{h}}$ point group merge into the A_g representation of the lower group $\mathbb{C}_{4\mathbb{h}}$. This signifies the breaking of the local vertical and diagonal reflection symmetries at the uranium sites in the HO phase. Similarly, the tiny intensity leakage into the RL scattering geometry measure the strength of orthorhombic distortion due to broken four-fold rotational symmetry.

When the reflection symmetries are broken, an A_{2g}-like interaction operator $\Psi_{\text{HO}} \equiv V\,|\mathbb{1}\rangle\,\langle\mathbb{0}|$ mixes the $|\mathbb{0}\rangle$ and $|\mathbb{1}\rangle$ states leading to two new local states: $|\mathbb{0}^{\text{L}}_{\text{HO}}\rangle \approx (1 - \frac{V^2}{2\omega_0^2})\,|\mathbb{0}\rangle - \frac{V}{\omega_0}\,|\mathbb{1}\rangle$ and $|\mathbb{0}^{\text{R}}_{\text{HO}}\rangle \approx (1 - \frac{V^2}{2\omega_0^2})\,|\mathbb{0}\rangle + \frac{V}{\omega_0}\,|\mathbb{1}\rangle$, with V being the interaction strength (*7*). A pair of such states cannot be transformed into one another by any remaining $\mathbb{C}_{4\mathbb{h}}$ group operators: a property known as chirality (or handedness). The choice of either the left-handed or the right-handed state on a given uranium site, $|\mathbb{0}^{\text{L}}_{\text{HO}}\rangle$ or $|\mathbb{0}^{\text{R}}_{\text{HO}}\rangle$, defines the local chirality in the HO phase (Fig. 1C). Notice that these two degenerate states both preserve the time reversal symmetry, carry no spin and contain the same charge, but differ only in handedness.

The same 1.6 meV sharp resonance has also been observed by inelastic neutron scattering at the commensurate crystal momentum, but only in the HO state (*17, 18, 30*). The Raman

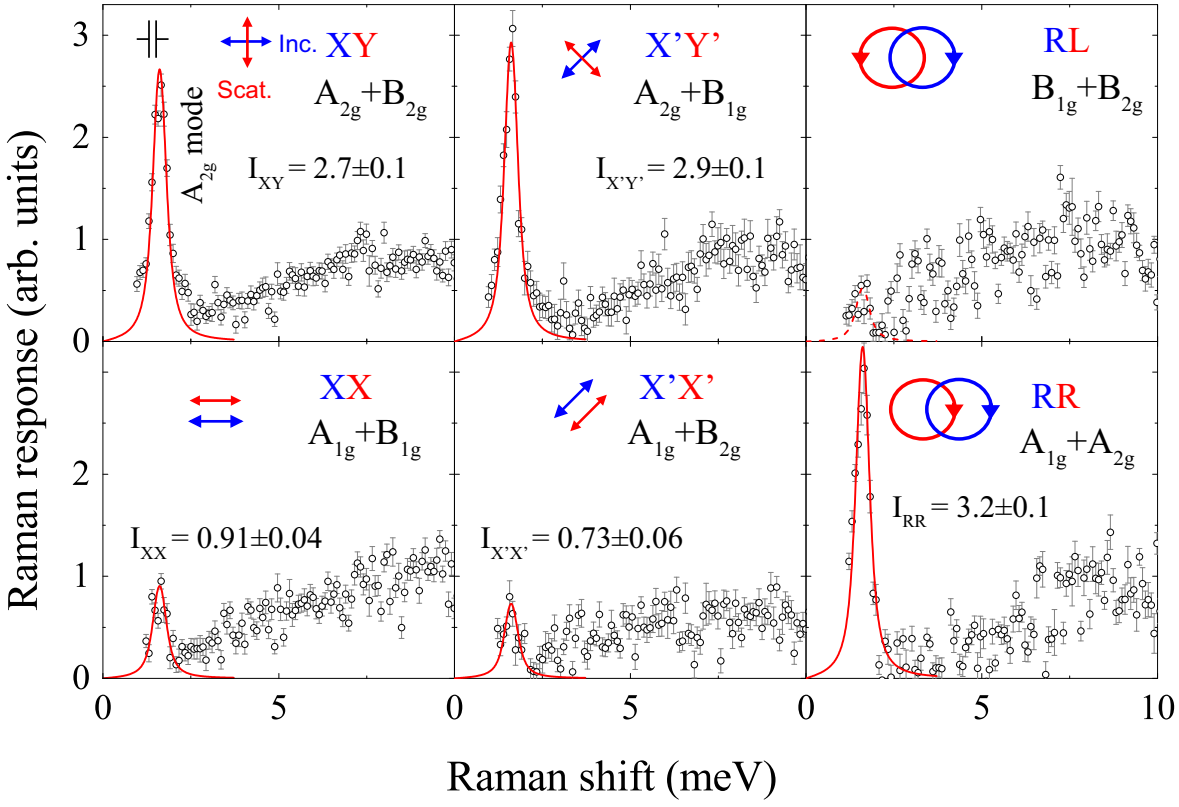

Figure 5: The Raman response in six proper scattering geometries at 7 K. The arrows in each panel show the linear or circular polarizations for incident (blue) and scattered (red) light. The six proper scattering geometries are denoted as $\mathbf{e}_s\mathbf{e}_i$ =XX, XY, X′X′, X′Y′, RR and RL, with $\mathbf{e}_i$ being the direction vector for incident light polarization, and $\mathbf{e}_s$ being the scattered light polarization. X=[100], Y=[010] are aligned along crystallographic axes, X′=[110], Y′=[1$\bar{1}$0] are aligned 45° to the *a*-axes, R=(X+iY)/$\sqrt{2}$ and L=(X-iY)/$\sqrt{2}$ are right and left circularly polarized light, respectively (*22*). The irreducible representations for each scattering geometry are shown within the $\mathbb{D}_{4h}$ point group. The data are shown in black circles, where the error bars show one standard deviation. The red solid lines are fits of the in-gap mode to a Lorentzian, and the fitted intensity using the method of maximum likelihood is shown in each panel. By decomposition, the in-gap mode intensity in each symmetry channels are: $\mathrm{I}_{\mathrm{A}_{2g}} = 2.6 \pm 0.1$, $\mathrm{I}_{\mathrm{A}_{1g}} = 0.7 \pm 0.1$, $\mathrm{I}_{\mathrm{B}_{1g}} = 0.3 \pm 0.1$, and $\mathrm{I}_{\mathrm{B}_{2g}} = 0.1 \pm 0.1$. The full width at half maximum of the in-gap mode is about 0.5 meV at 7 K (deconvoluted with instrumental resolution of 0.15 meV, shown in the XY panel).

measurement proves that this resonance is a long-wavelength excitation of A_{2g} character. The appearance of the same resonance in the neutron scattering at different wavelength, corresponding to the *c*-axis lattice constant, requires HO to be a staggered alternating electronic order in c direction. Such order with alternating left and right handed states at the uranium sites for neighboring basal planes, has no modulation of charge or spin, and does not couple to tetragonal lattice, hence it is hidden to all probes but scattering in A_{2g} symmetry. We reveal this hidden order to be a chirality density wave depicted in figure 1D.

The chirality density wave doubles the translational periodicity of the paramagnetic phase, hence it folds the electronic Brillouin zone, as recently observed by angle-resolved photoemission spectroscopy (*31*). It also gives rise to an energy gap, as previously observed in optics (*12–14*) and tunneling experiments (*15, 32*), and shown in figure 4 to originate in expelling the continuum of A_{2g} excitations. The sharp (0.3 meV) resonance is explained by excitation from the ground state, which posses chirality density wave staggering $|\mathbb{0}^{\mathrm{L}}_{\mathrm{HO}}\rangle$ and $|\mathbb{0}^{\mathrm{R}}_{\mathrm{HO}}\rangle$, to the excited state depicted in figure 1D, which staggers $|\mathbb{0}^{\mathrm{L}}_{\mathrm{HO}}\rangle$ and $|\mathbb{1}_{\mathrm{HO}}\rangle$ (*22*).

A local order parameter of primary A_{2g} symmetry, breaking vertical/diagonal reflections, with subdominant B_{1g} component, breaking four-fold rotational symmetry, can be expressed in terms of the composite hexadecapole local order parameter of the form:

$$\pm V[(J_x - J_y)(J_x + J_y)(J_xJ_y + J_yJ_x) + (J_xJ_y + J_yJ_x)(J_x + J_y)(J_x - J_y)]$$

where J_x, J_y are in-plane angular momentum operators (*7, 22*). A spatial order alternating the sign of this hexadecapole for neighboring basal planes is the chirality density wave (see Fig. 1D) that consistently explains the HO phenomena as it is observed by Raman and neutron scattering (*16–18, 30*), magnetic torque (*19*), X-ray diffraction (*20*), and other data (*11–14, 31*). Our finding is a new example of exotic electronic ordering, emerging from strong interaction among *f* electrons, which should be a more generic phenomenon relevant to other intermetallic compounds.

References and Notes

1. G. R. Stewart, *Rev. Mod. Phys.* **56**, 755 (1984).

2. P. Santini, *et al.*, *Rev. Mod. Phys.* **81**, 807 (2009).

3. T. T. M. Palstra, *et al.*, *Phys. Rev. Lett.* **55**, 2727 (1985).

4. M. B. Maple, *et al.*, *Phys. Rev. Lett.* **56**, 185 (1986).

5. P. Santini, G. Amoretti, *Phys. Rev. Lett.* **73**, 1027 (1994).

6. P. Chandra, P. Coleman, J. A. Mydosh, V. Tripathy, *Nature (London)* **417**, 831 (2002).

7. K. Haule, G. Kotliar, *Nature Phys.* **5**, 796 (2009).

8. S. Elgazzar, J. Rusz, M. Amft, P. M. Oppeneer, J. A. Mydosh, *Nature Mater.* **8**, 337 (2009).

9. H. Ikeda, *et al.*, *Nature Phys.* **8**, 528 (2012).

10. P. Chandra, P. Coleman, R. Flint, *Nature (London)* **493**, 621 (2013).

11. J. A. Mydosh, P. M. Oppeneer, *Rev. Mod. Phys.* **83**, 1301 (2011). And references therein.

12. D. A. Bonn, J. D. Garrett, T. Timusk, *Phys. Rev. Lett.* **61**, 1305 (1988).

13. J. S. Hall, *et al.*, *Phys. Rev. B* **86**, 035132 (2012).

14. W. T. Guo, *et al.*, *Phys. Rev. B* **85**, 195105 (2012).

15. P. Aynajian, *et al.*, *Proc. Nat. Acad. Sci. USA* **107**, 10383 (2010).

16. C. Broholm, *et al.*, *Phys. Rev. B* **43**, 12809 (1991).

17. C. R. Wiebe, *et al.*, *Nature Phys.* **3**, 96 (2007).

18. F. Bourdarot, *et al.*, *J. Phys. Soc. Jpn.* **79**, 064719 (2010).

19. R. Okazaki, *et al.*, *Science* **331**, 439 (2011).

20. S. Tonegawa, *et al.*, *Nature Commun* **5** (2014).

21. J. R. Jeffries, K. T. Moore, N. P. Butch, M. B. Maple, *Phys. Rev. B* **82**, 033103 (2010).

22. See supporting materials.

23. B. S. Shastry, B. I. Shraiman, *Int. J. Mod. Phys. B* **5**, 365 (1991).

24. J. A. Koningstein, O. S. Mortensen, *Nature* **217**, 445 (1968).

25. H. Rho, M. V. Klein, P. C. Canfield, *Phys. Rev. B* **69**, 144420 (2004).

26. S. L. Cooper, M. V. Klein, M. B. Maple, M. S. Torikachvili, *Phys. Rev. B* **36**, 5743 (1987).

27. L. N. Ovander, *Optics and Spectroscopy* **9**, 302 (1960).

28. S. C. Riggs, *et al.*, *ArXiv e-prints* (2014).

29. M. Klein, *Light Scattering in Solids I*, M. Cardona, G. Güntherodt, eds. (Springer-Verlag, Berlin, 1983), pp. 169–172.

30. F. Bourdarot, B. Fåk, K. Habicht, K. Prokeš, *Phys. Rev. Lett.* **90**, 067203 (2003).

31. R. Yoshida, *et al.*, *Sci. Rep.* **3** (2013).

32. A. R. Schmidt, *et al.*, *Nature (London)* **465**, 570 (2010).

33. **Acknowledgments** We thank J. Buhot, P. Chandra, P. Coleman, G. Kotliar, M.-A. Méasson, D.K. Morr, L. Pascut, A. Sacuto and J. Thompson for discussions. G.B. and V.K.T. acknowledge support from the US Department of Energy, Office of Basic Energy Sciences,

Division of Materials Sciences and Engineering under Award DE-SC0005463. H.-H.K. acknowledges support from the National Science Foundation under Award NSF DMR-1104884. K.H. acknowledges support by NSF Career DMR-1405303. W.-L. Z. acknowledges support by ICAM (NSF-IMI grant DMR-0844115). Work at Los Alamos National Laboratory was performed under the auspices of the US Department of Energy, Office of Basic Energy Sciences, Division of Materials Sciences and Engineering.